Progress In Electromagnetics Research Letters, Vol. 128, 26–34, 2025

PIER Letters

(Received 6 August 2025, Accepted 31 October 2025, Scheduled 12 November 2025)

Research on Orbital Angular Momentum of Low-Profile Ultra-Wideband Reflective Metasurface

Rongxian Bai, Minquan Li*, Shuang Xiao, Xin Qu, Chen Li,
Guocui Zhu, Yongkang Yuan, Boyan Zhang, and Zhonghui Li

Information Materials and Intelligent Sensing Laboratory of Anhui Province, Anhui University, Hefei 230601, China

ABSTRACT: With the increasing demand for high-capacity communication systems, vortex beams endowed with orbital angular momentum (OAM) have emerged as a promising candidate for enhancing channel capacity of communication systems. Persistent limitations of conventional OAM generators, such as narrow bandwidth, single-mode constraints, and decreased purity in high-order OAM modes are addressed. In this work, by combining Pancharatnam-Berry (PB) phase theory and an equivalent circuit, we design a metasurface unit with gradient phase compensation. The metasurface unit overcomes the bandwidth limits of resonant structures, achieving 360° linear phase modulation at 8–20 GHz (85.7% relative bandwidth) and allowing vortex waves with multiple OAM modes and high-order mode purity. Quantitative assessment of modal purity via OAM spectral decomposition demonstrates exceptional agreement between experimental measurements and full-wave simulations, thus corroborating the theoretical framework and underscoring the potential of the methodology for practical implementation.

1. INTRODUCTION

The investigation of orbital angular momentum (OAM) in vortex electromagnetic waves originated from the foundational work of Allen et al. in 1992 [1], and then other studies have discovered the channel capacity advantage of OAM by different OAM modes comparing spin angular momentum (SAM). Therefore, different OAM vortex beams have made significant progress in micron and nano manipulation [2, 3], quantum information systems [4, 5], and high-capacity wireless communications [6].

OAM generation techniques have progressed rapidly in the optical regime. A major milestone for the microwave band was reached in 2007 when Thidé et al. demonstrated a circular array antenna-based phase modulation approach, achieving the first experimental realization of tapered vortex beams with different OAM patterns [7]. Subsequent development in the microwave domain was marked by the implementation of parabolic antenna configurations in 2012, which enabled the generation of OAM waves with an OAM mode of $l = 1$ and experimentally verified the ability of two orthogonal vortex waves to be transmitted independently [8].

Spiral phase plates (SPPs) [9, 10] and antenna arrays [11–13] have become the main mechanisms of generation of OAM. Although azimuth-dependent phase modulation is achieved through helical geometries in SPPs, the generation of higher-order modes necessitates intricate three-dimensional fabrication processes. However, a discrete structure in a stepped structure [14] or using a planarized SPP configuration [10] can simplify the fabrication process. Circular antenna arrays are another approximation for generating OAM vortex waves with discrete currents based on Nyquist theory.

Based on Pancharatnam-Berry (PB) phase theory [15–18], it is possible to generate abrupt changes based on the phase, amplitude, or polarization of an electromagnetic wave. Through controlled cell rotation to induce geometric phase modulation, single-layer metasurface architectures enable broadband, low-profile OAM generation, as exemplified by V-shaped elements [16, 17] and square-loop configurations [18]. Compared with its multilayer counterparts [19, 20], the single-layer implementation demonstrates superior compatibility with wireless communication systems [15]. Since phase modulation depends only on the adjustment of the orientation angle, it is possible to achieve both high integration and wide operating bandwidth.

OAM mode multiplexing technology, as a potential 6G communication technique, utilizes the orbital angular momentum property of electromagnetic waves. By leveraging the orthogonality between different modes, it enables channel distinction within the same spatial domain, allowing independent transmission of multiple signals without interference. This approach promises significant improvement in spectral efficiency. Meanwhile, with the growing demand for broadband and miniaturized wave-control devices, conventional geometrically configured components (e.g., lenses, parabolic reflectors, and antenna arrays) have shown limitations. For instance, low-profile designs can be integrated into mobile platforms and handheld devices; broadband capability supports high-speed data transmission meeting practical communication requirements; furthermore, vortex wave generators supporting high-order modes present a highly promising technical pathway for enhancing channel capacity in communication systems.

---

* Corresponding author: Minquan Li (AHU411MHz@hotmail.com).

doi:10.2528/PIERL25080603

Published by THE ELECTROMAGNETIC ACADEMY

This research aims to develop a single-layer low-profile reflective metasurface leveraging the PB phase principle and equivalent circuit for the modulation of OAM of circularly polarized waves in the microwave regime. We propose an innovative metasurface architecture that demonstrates boardband OAM generation capability from 8 to 20 GHz with multiple OAM modes and high-order mode purity. Quantitative evaluation via OAM spectral decomposition reveals close agreement between experimental measurements and numerical simulations, thereby confirming the theoretical validity and engineering applicability of the proposed methodology.

2. DESIGN THEORY METHODOLOGY

Jones matrix [21, 22], which can accurately describe the incident and reflected fields of anisotropic metasurface elements, where matrix R_{xy} not only reflects the linear relationship between the reflected and incident waves but also contains information about the transition of the wave's polarization state. The process of SAM to OAM can be demonstrated by [23]:

$$r_{ll}(\alpha) = 0.5[(r_{xx} - r_{yy}) + j(r_{xy} + r_{yx})]e^{-2j\alpha} \tag{1}$$

$$r_{lr}(\alpha) = 0.5\Big[(r_{xx} + r_{yy}) + j\,(r_{yx} - r_{xy})\Big] \tag{2}$$

$$r_{rl}(\alpha) = 0.5\big[(r_{xx} + r_{yy}) - j\big(r_{yx} - r_{xy}\big)\big] \tag{3}$$

$$r_{rr}(\alpha) = 0.5\big[(r_{xx} - r_{yy}) - j\big(r_{xy} + r_{yx}\big)\big]e^{2j\alpha} \tag{4}$$

The co-polarized reflection coefficients r_{xx} and r_{yy} are defined as the reflection responses under linearly polarized (LP) illumination with x- and y-polarization states, respectively. On circular polarization basis, r_{ll} and r_{rr} correspond to left-handed circularly polarized (LCP) and right-handed circularly polarized (RCP) co-polarized reflections, respectively. The cross-polarization conversion is quantified by r_{yx}, r_{xy}, r_{lr}, and r_{rl}, whose complex values encode both reflection efficiency and phase modulation characteristics during orthogonal polarization transitions.

As demonstrated in (1) and (4), the geometric phase compensation induced by unit cell rotation through angle α exhibits a functional dependence on co-polarized reflection coefficients. Precise wavefront engineering is achieved through controlled angular adjustment $\Delta\alpha$, in which the reflected wave phase is deterministically tailored to allow manipulation of the electromagnetic wavefront.

Reflection efficiency constitutes a critical consideration in metasurface unit cell design and implementation. Under the condition of xoz or yoz plane mirror symmetry, the cross-polarization coefficients satisfy $r_{yx} = r_{xy} = 0$ [22], allowing a significant simplification of the governing equations.

$$r_{ll}(\alpha) = 0.5(r_{xx} - r_{yy})e^{-2j\alpha} \tag{5}$$

$$r_{lr}(\alpha) = 0.5\big(r_{xx} + r_{yy}\big) \tag{6}$$

$$r_{rl}(\alpha) = 0.5\big(r_{xx} + r_{yy}\big) \tag{7}$$

$$r_{rr}(\alpha) = 0.5\big(r_{xx} - r_{yy}\big)e^{2j\alpha} \tag{8}$$

For lossless metasurfaces, energy conservation dictates $|r_{yy}|^2 + |r_{xy}|^2 = 1$ and $|r_{xx}|^2 + |r_{yx}|^2 = 1$, thus requiring $|r_{xx}| = |r_{yy}| = 1$ under ideal conditions. To achieve maximum reflection efficiency, the unit cell design must satisfy [23]:

$$\arg\left(r_{xx}(\omega)\right) - \arg\left(r_{yy}(\omega)\right) \approx \pm\pi \tag{9}$$

Conventional patch or strip array configurations are limited by single-polarization surface impedance responses, which poses challenges to achieving broadband high-efficiency polarization conversion through geometric phase modulation within single-layer dielectric architectures. In [24–27], effective equivalent lumped circuit models have been established for some common periodic sub-wavelength structures, such as metal strip grids (equivalent inductance), arrays of metal patches (equivalent capacitance), and square ring arrays (series LC circuit). In contrast, square-loop metasurface elements provide multidimensional tuning capabilities via equivalent series LC-resonant circuit topologies. In this work, a symmetric rectangular loop topology is developed in Fig. 1, leveraging geometric phase engineering to enhance the polarization conversion performance.

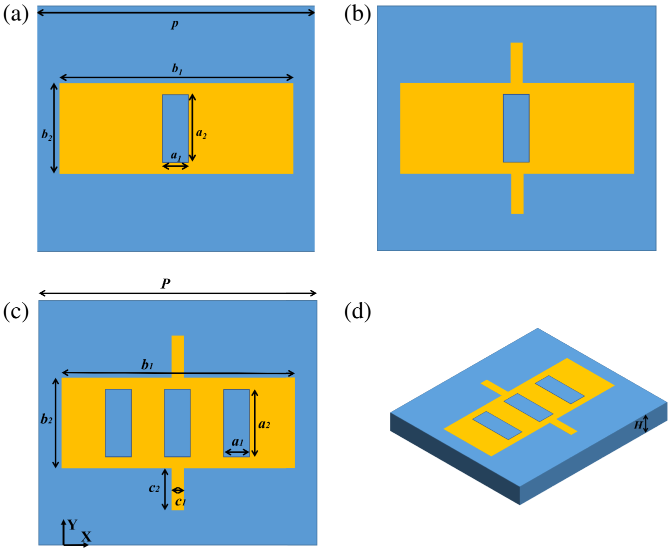

FIGURE 1. Metasurface unit: (a) Unit 1; (b) Unit 2; (c) Unit 3; (d) Side view of unit 3.

The equivalent circuit model of the proposed single-layer metasurface is presented in Fig. 2, with the reflection coefficient derived from transmission line theory:

$$r_{xx} = \frac{Z_i^{in} - Z_0}{Z_i^{in} + Z_0} \ldots = |r_{xx}|e^{j\phi x}(i = 1) \tag{10}$$

$$r_{yy} = \frac{Z_i^{in} - Z_0}{Z_i^{in} + Z_0} \ldots = |r_{yy}|\,e^{j\phi y}(i = 2) \tag{11}$$

where $Z_0 = 377\,\Omega$ is the impedance of the free space wave; $Z_d = Z_0/\sqrt{\varepsilon_r} = 231.6\,\Omega$ is the impedance of the equivalent transmission line; and the metallic ground is equivalent to the boundary condition of the ideal electrical conductor. The

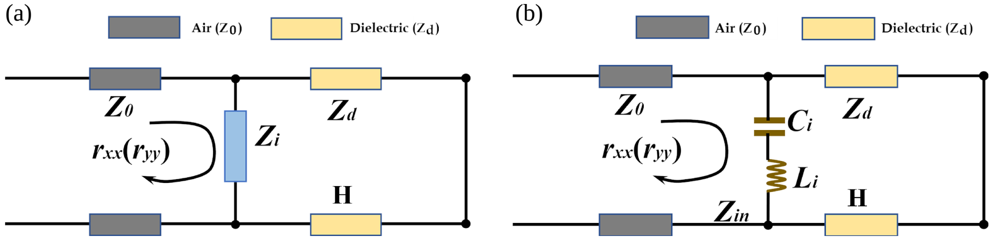

FIGURE 2. (a) Transmission line (TL)-based equivalent model of monolayer metasurface metaelement. (b) Lumped-element equivalent circuit of deformed square loop metasurface for polarization conversion.

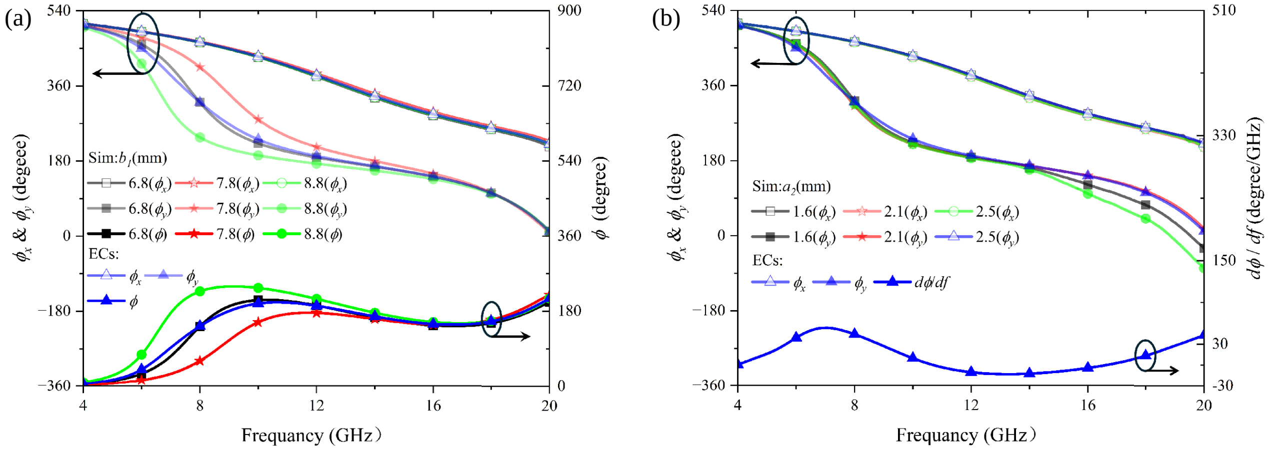

FIGURE 3. Simulation (Sim) and equivalent circuits (ECs) models are calculated. Simulation results of ϕ_x and ϕ_y as a function of (a) b_1 and (b) a_2. Other parameters are (a) $b_2 = 2.6\,\text{mm}$, $a_1 = 0.8\,\text{mm}$, $a_2 = 2.1\,\text{mm}$, and $p = 10\,\text{mm}$ and (b) $b_1 = 7.8\,\text{mm}$, $b_2 = 2.6\,\text{mm}$, $a_1 = 0.8\,\text{mm}$, and $p = 10\,\text{mm}$.

equivalent surface impedance of the metasurface metal layer Z_i^{in} is satisfied:

$$Z_i^{in} = \frac{jZ_d\tan(\beta h) * \left(j\omega L_i + \frac{1}{j\omega C_i}\right)}{jZ_d\tan(\beta h) + j\omega L_i + \frac{1}{j\omega C_i}} \tag{12}$$

where β is the medium propagation constant, and ϕ_x and ϕ_y are the orthogonally polarized reflection phases, respectively. The phase difference is defined as follows:

$$\phi = \phi_x - \phi_y \tag{13}$$

The phase difference is defined to achieve broadband geometric phase modulation as follows:

$$\phi(f) = \pi \tag{14}$$

ϕ has to satisfy the following condition for frequencies ranging from ω_1 to ω_2:

$$\frac{d\phi}{d\omega} \approx 0, \quad \omega \in (\omega_1, \omega_2) \tag{15}$$

Substituting (10)–(14) into (15), one can derive a set of effective capacitance and inductance values. The corresponding results of the EC model are shown in Fig. 2. The corresponding metasurface unit is illustrated in Fig. 1(a). Within the operating bandwidth, the phase difference ϕ remains around 180 ± 40, while the phase variation rate dϕ/df is maintained within ±30°/GHz. These results confirm that the proposed model can achieve a broadband 180° phase difference between the reflection coefficients for the x- and y-polarizations. The absence of significant resonance within the operating band ensures minimal variation in the reflection phases ϕ_x and ϕ_y, which is crucial to achieve wideband and high-efficiency characteristics.

By adjusting the geometric parameters of the deformed square loop structure, the desired capacitance and inductance values can be obtained. Variations in parameter b_1 mainly affect the coupling capacitance C_2 between adjacent unit cells along the y-direction, consequently influencing the y-polarized reflection phase ϕ_y, as shown in Fig. 3(a). Similarly, changes in parameter a_2 mainly alter inductance L_2, thereby modifying ϕ_y, as illustrated in Fig. 3(b). The x-polarized reflection phase ϕ_x can be correspondingly controlled by adjusting parameters a_1 and b_2. The close agreement between the simulated reflection phase of the meta-atom and the predictions from the EC model validates the proposed design methodology.

3. METASURFACE DESIGN

The initial prototype (unit 1), designed using equivalent circuit modeling, achieves a co-polarized energy conversion efficiency > 0.8 over 7.38–20.02 GHz with pronounced fluctuations in the reflection coefficient. The reconstruction of structural parameters yields unit 2, which extends the operational

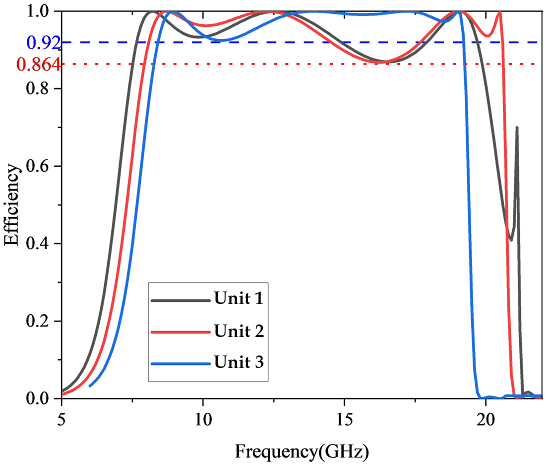

FIGURE 4. Conversion efficiencies of ultrawideband meta-surface units. Unit 1: Efficiency > 0.8; Unit 2: Efficiency > 0.864; Unit 3: Efficiency > 0.92.

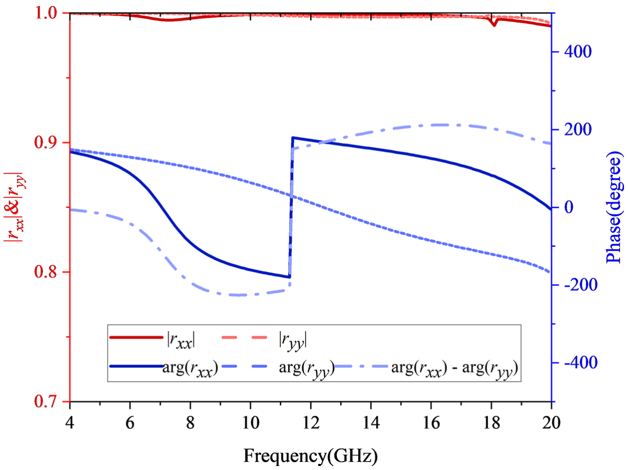

FIGURE 5. Reflection characteristics of ultra-wideband meta-atom under LP illumination.

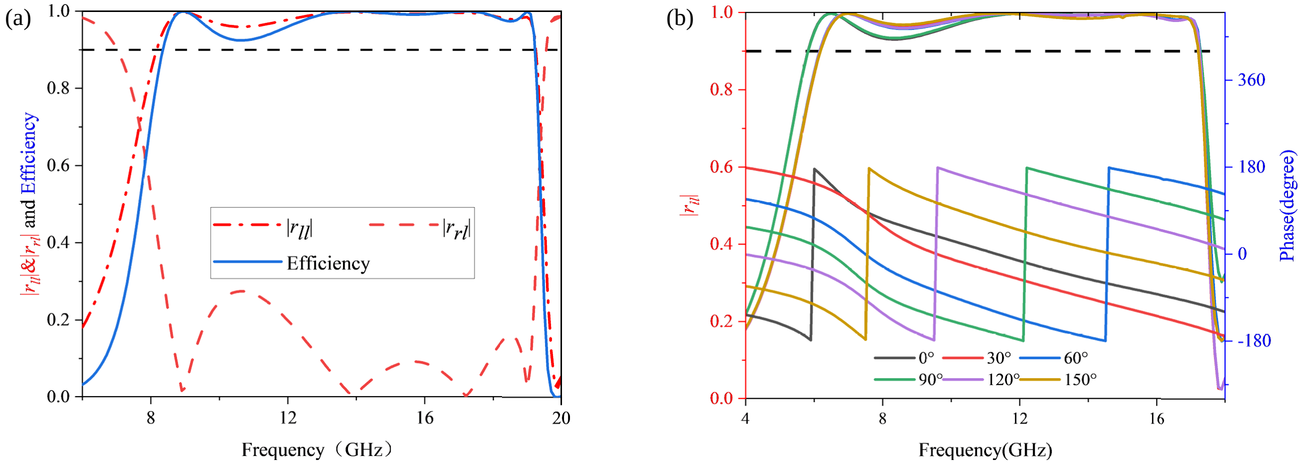

FIGURE 6. Reflection characteristics of ultra-wideband meta-atom under (a) CP illumination. (b) Reflection characteristics of ultrawideband meta-atom with different rotation angles under CP wave illumination.

bandwidth to 7.94–20.61 GHz while enhancing the conversion efficiency to 0.864 and suppressing the degradation of efficiency at 21 GHz. Through iterative refinement, unit 3 shown in Fig. 1(c) and Fig. 1(d) is subsequently developed $p = 10\,\text{mm}$, $b_1 = 8.8\,\text{mm}$, $b_2 = 2.6\,\text{mm}$, $a_1 = 0.8\,\text{mm}$, $a_2 = 2\,\text{mm}$, $c_1 = 0.4\,\text{mm}$, $c_2 = 1.5\,\text{mm}$, substrate thickness $H = 3\,\text{mm}$ with relative permittivity $\varepsilon_\text{r} = 2.65$. As quantitatively validated in Fig. 4, the proposed method shows a superior conversion efficiency relative to previous iterations.

$$\mathit{Efficiency} = |r_{ll}|^2 \tag{16}$$

4. SIMULATION AND MEASUREMENT RESULTS

4.1. Metasurface Cell Simulation Results

Electromagnetic simulations conducted in High Frequency Structure Simulator (HFSS) (Fig. 5 and Fig. 6) demonstrate that the unit achieves exceptional co-polarized reflection performance over 7.85–20.58 GHz (relative bandwidth $> 92\%$), characterized by quasi-unity reflection coefficients for x and y polarizations with orthogonal phase difference maintained at approximately 180°, satisfying broadband geometric phase tuning requirements.

The circular polarization conversion efficiency is quantitatively evaluated in Fig. 5.

Periodic boundary condition analysis (Fig. 5) reveals an effective relative bandwidth approaching 90% in conversion efficiency $> 90\%$, significantly better than double-arrow metasurfaces (12–18 GHz, 40% bandwidth) [28]. Phase linearity evaluation (Fig. 6(b)) confirms that the full-band co-polarized reflection coefficient is stable above 0.92 when the rotation angle of the unit is varied, and the phase linearity is in high agreement with the theoretical prediction, establishing the foundation for high-purity OAM metasurface realization.

4.2. Numerical Near-Field Results of Boardband Metasurface

Using PB phase theory, a 16×16 periodic metasurface array is developed (Fig. 7) to generate OAM beams with topologi-

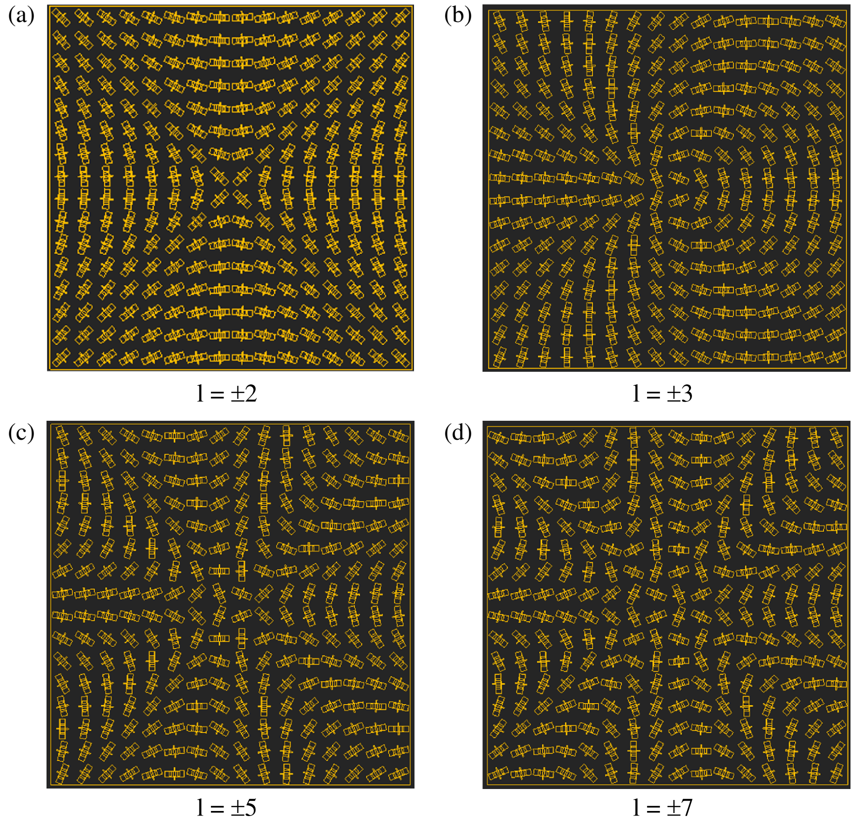

l = ±2 l = ±3 l = ±5 l = ±7

FIGURE 7. Electromagnetic modes of the periodically arranged vortex-wave metasurface schematic.

cal charges $l = \pm 2$, $l = \pm 3$, $l = \pm 5$ and $l = \pm 7$. Phase modulation is implemented through unit cell rotation according to $\alpha = l\phi/2$, where ϕ denotes the azimuthal angle, with the charge polarity determined by the incident circular polarization handedness.

An electromagnetic model is established using the HFSS simulation platform incorporating left-handed (LH) circularly polarized plane-wave excitation and floquet boundary conditions to compute near-field radiation patterns. The proposed metasurface successfully generates vortex waves in the $l = -3$ mode, as evidenced by the reflected field polarization decomposition (LH/RH components in Fig. 8). The distributions of the electric field amplitude in the near field at an observation distance of 100 mm (over a 180 mm × 180 mm scan area) exhibit characteristic toroidal profiles, which confirms the successful synthesis of the vortex wave mode.

To quantify the modal purity of OAM, the vortex spectral decomposition method [28] was applied using the mode expansion equation.

$$A_l = \frac{1}{2\pi}\int_0^{2\pi} E(\varphi)\, e^{-jl\varphi} d\varphi \tag{17}$$

In the near-field simulation data, the complex amplitude distribution $E(\phi)$ is extracted in the peak loop domain of the electric field. The modal spectral coefficients A_l for each order are calculated, and their corresponding energy weights are normalized.

$$\text{energy weight} = \frac{|A_l|}{\sum_{l'=-7}^{7} |A_{l'}|} \tag{18}$$

Figure 8 shows the scattering field distributions of a board-band metasurface with the OAM mode of $l = -3$ operating at six discrete frequencies: 9 GHz, 11 GHz, 13 GHz, 15 GHz, 17 GHz, and 19 GHz. Experimental observations reveal that, under the LH circular polarization, the electric-field amplitude exhibits a distinct annular distribution. Currently, the helical phase profiles at all six frequencies demonstrate three complete rotational cycles, which aligns with the expected vortex wave mode for the $l = -3$ design. The precise phase distribution confirms the metasurface's capability to convert incident waves into vortex waves with the designated topological charge, ensuring compliance with the prescribed beam mode and functional specifications.

The cross-polarized RH component exhibits significantly lower amplitude across all tested frequencies, indicating effective suppression of undesired RH polarization. This highlights the metasurface's polarization selectivity and operational efficiency, ensuring predominant preservation of the LH component while minimizing RH influence, thereby achieving high-efficiency mode conversion.

4.3. Generation and Analysis of High-Order Vortex Waves

Figure 9 presents experimental and numerical simulation results that demonstrate how metasurfaces with varying modes

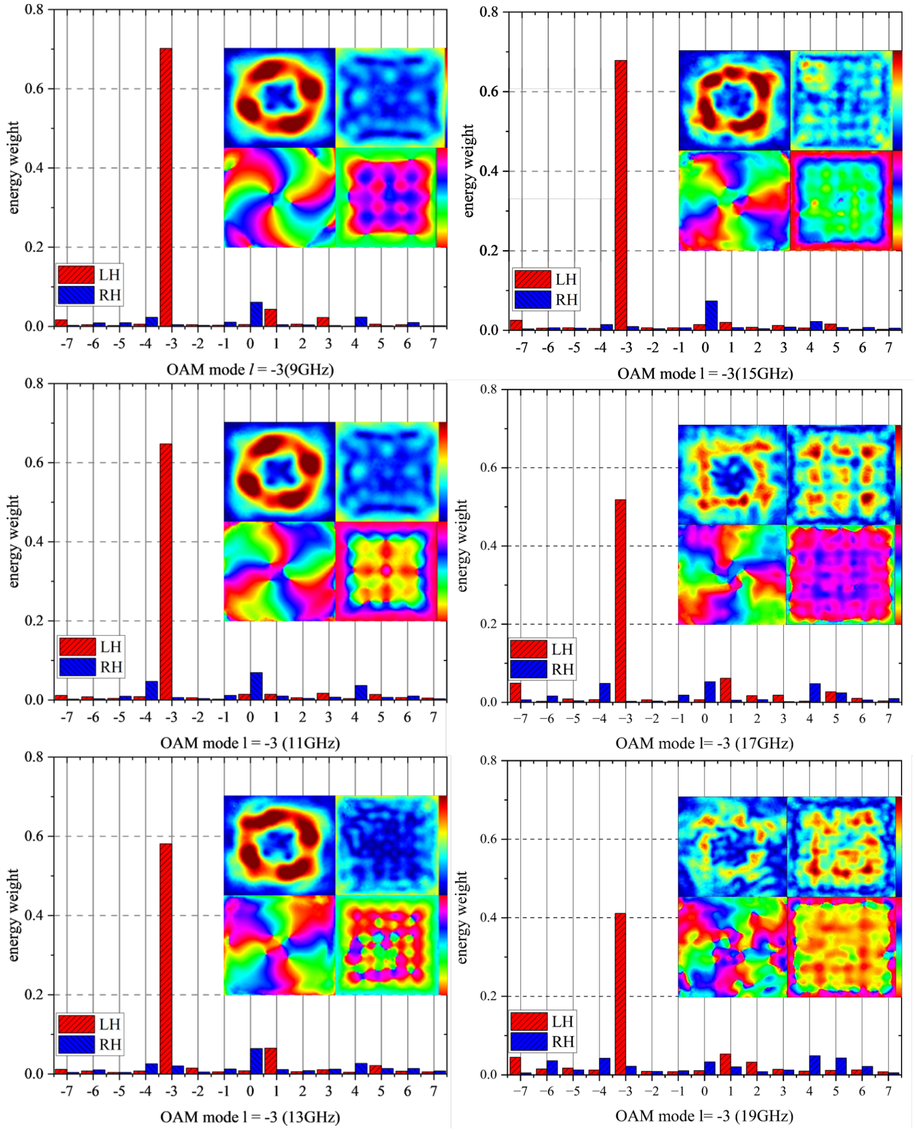

FIGURE 8. Near-field characterization and spectral evaluation of synthesized $l = -3$ OAM beams across discrete frequency points, with a 180 mm × 180 mm sampling plane positioned 100 mm from the metasurface.

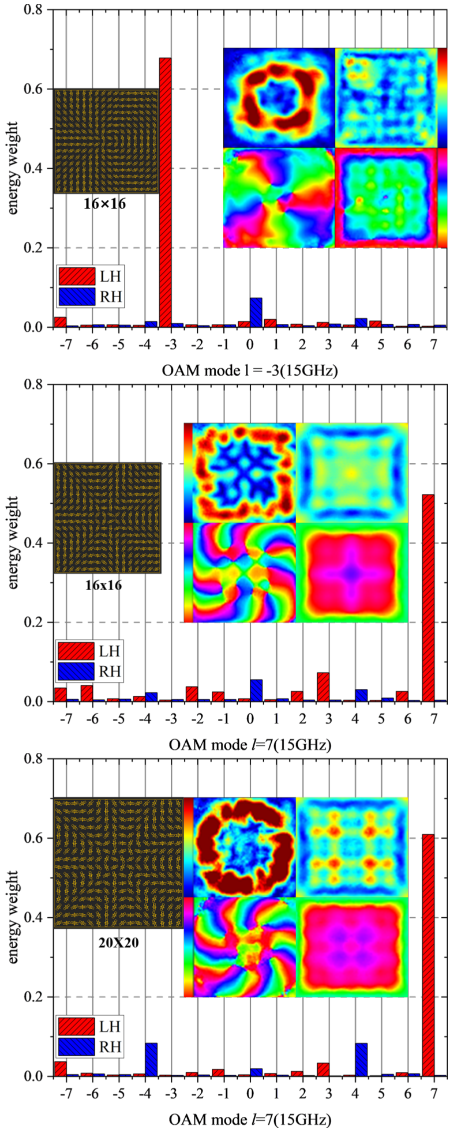

FIGURE 9. Near-field spectral response of $l = -3$ OAM beam generated by 16×16-element metasurface array, $l = 7$ OAM mode generated by 16×16-element metasurface array, $l = 7$ OAM mode generated by 20×20-element metasurface array.

and dimensions influence the characteristics of the vortex field. These results validate the capability and efficacy of metasurfaces in generating electromagnetic waves with OAM.

In Fig. 9, the geometry of the metasurface, the corresponding electromagnetic field distribution, and the calculated OAM spectrum are shown. The OAM spectrum confirms the metasurface's ability to generate the desired vortex wave with high fidelity. Furthermore, Fig. 9 compares the performance of a metasurface of higher-order mode ($l = 7$) with its field results. A reduction in mode purity and an increase in the divergence angle are observed as the target order of the OAM mode increases, highlighting the challenge of balancing size constraints and mode purity when designing higher-order modes.

Figure 9 shows that a 20×20 metasurface improves the quality generated by the $l = 7$ vortex mode compared to smaller configurations. The increased value allows smoother azimuthal phase gradients that suppress secondary modes and enhance spectral purity. The expanded design reduces beam divergence by better aligning the wave vectors and focusing the OAM. This behavior aligns with the spatial-frequency trade-off in Fourier optics, where larger apertures inherently refine phase resolution and angular confinement. Although these trends confirm the necessity of aperture scaling for high-order mode generation, a comprehensive quantitative framework would require controlled comparisons across varied topological charges and array sizes.

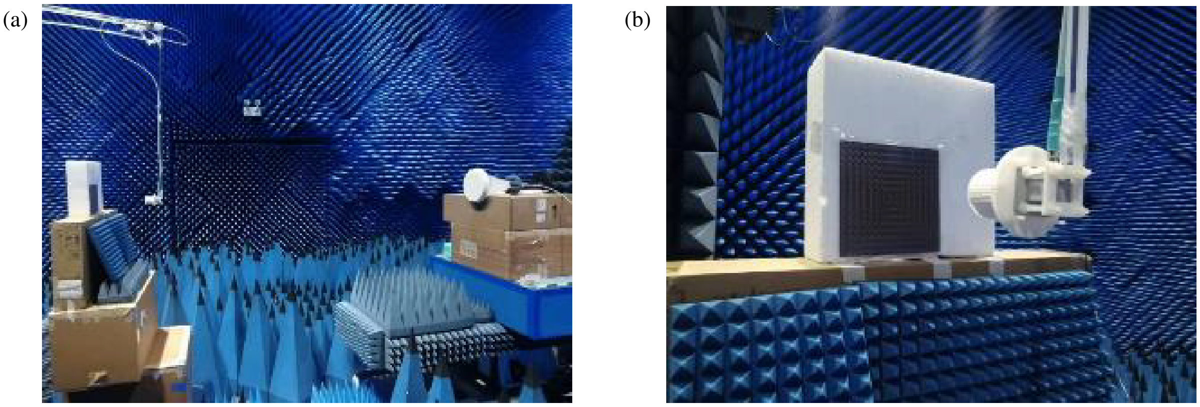

FIGURE 10. The photograph of corresponding experimental system: (a) Longdistance. (b) Short-distance.

4.4. Metasurface Machining Actual Test and Verification

A near-field scanning-based quantitative characterization system was developed to evaluate the OAM generation performance of the metasurface prototype, utilizing vortex wave analysis as validation metric (Fig. 10). The experimental setup incorporated a 600 mm × 600 mm near-field scanning plane positioned 350 mm from the metasurface aperture, with left-hand circularly polarized quasi-planar wave excitation achieved through a standard gain horn antenna integrated with two polarization converters. Spatial sampling of electric-field complex amplitudes is performed via an open-ended waveguide probe mounted on a three-axis robot arm positioning system, enabling full-vector near-field amplitude and phase reconstruction.

As demonstrated in Fig. 11, the experimental electric field amplitude distribution exhibits a characteristic toroidal null profile within 10 GHz, 10.5 GHz, 11 GHz, and 11.5 GHz, with the phase gradient completing two full 2π cycles over azimuthal rotation (topological charge $l = 2$) confirming the fundamental properties of OAM beams. The normalized energy-weighted modal decomposition reveals the purity of the dominant mode $l = 2$. The remaining modes are multiples of 2, with fewer odd modes, and the higher-order modes account for a smaller proportion of the total energy distribution. The primary cause of this discrepancy is that the waves incident on the metasurface during the test are not plane waves in the strict sense and are not incident vertically, with some angular deviation, while the center points are not perfectly aligned, so an error occurs. However, the percentage of mode purity 2 is significantly higher than those in the other modes.

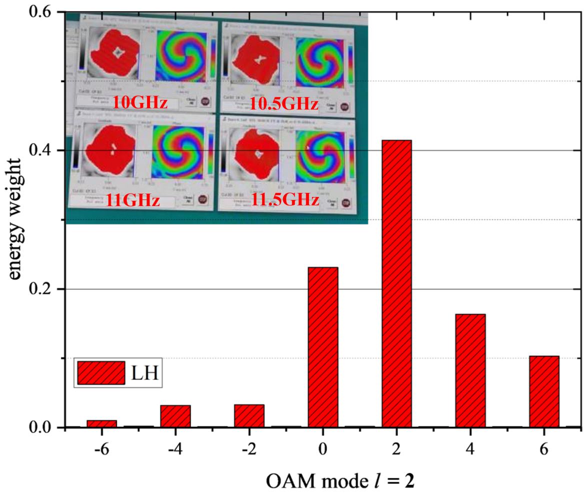

FIGURE 11. Spatiotemporal characterization of reflected OAM beams ($l = 2$): Amplitude-phase profiles and reflection response of a metasurface element under left-hand circularly polarization at 10 GHz, 10.5 GHz, 11 GHz, and 11.5 GHz.

Further analysis reveals that these discrepancies stem from the metasurface's electromagnetic wave manipulation capabilities and bandwidth performance. The design and optimization of the metasurface structural parameters are critical to achieving high-efficiency, broad-bandwidth vortex wave transmission. Building on this foundation, the metasurface design can be further refined to improve electric field distributions at targeted frequencies, thereby enhancing its performance and expanding.

Based on the comparative analysis presented in Table 1, the proposed reflectarray metasurface for OAM generation demonstrates a superior advantage in terms of operational bandwidth. Specifically, the proposed design achieves a bandwidth of 85.7%, which substantially outperforms all other state-of-the-art OAM antennas listed in the table, whose bandwidths range

TABLE 1. Simplified comparison of OAM antenna performance.

Ref.	Type	Freq. (GHz)	BW (%)	OAM mode	Mode purity
[29]	R	10	20.0	$l = \pm 1$	NA
[30]	R	30	21.7	$l = \pm 1$	≥ 62.6
[31]	R	12	22.5	$l = \pm 1$	≥ 77.5
[32]	T	30	33.3	$l = \pm 1$	≥ 72.0
This work	R	12	85.7	$l = \pm 3$	≥ 70.5

Note: R = Reflectarray, T = Transmitarray,
BW = Bandwidth, NA = Not available

from 20.0% to 33.3%. This exceptional bandwidth is a critical achievement for practical high-data-rate communication systems utilizing OAM multiplexing. Furthermore, this boardband performance is achieved while maintaining a high-order OAM mode ($l = \pm 3$), which is more challenging to generate with purity over a wide frequency range. The proposed antenna maintains a mode purity of $\geq 70.5\%$. Therefore, the data in Table 1 conclusively highlights that the proposed design successfully balances ultra-wideband functionality with the stable generation of a high-order OAM mode.

5. SUMMARY

In this work, by combining the PB phase theory and equivalent circuit, we design a metasurface unit with gradient phase compensation. This approach overcomes the bandwidth limits of resonant structures, achieving 360° linear phase modulation from 8 to 20 GHz (85.7% relative bandwidth) and allowing vortex waves with multiple OAM modes and high-order modes. Quantitative assessment of modal purity via OAM spectral decomposition demonstrates exceptional agreement between experimental measurements and full-wave simulations, thus corroborating the theoretical framework and underscoring the potential of the methodology for practical implementation. The proposed technology provides a compact solution for the generation of OAM beams in high capacity wireless communication systems and multidimensional radar imaging applications.

ACKNOWLEDGEMENT

This work was supported in part by Anhui Province Higher Education Science Research Project under Grant 2022AH050070.

REFERENCES

[1] Allen, L., M. W. Beijersbergen, R. J. C. Spreeuw, and J. P. Woerdman, “Orbital angular momentum of light and the transformation of Laguerre-Gaussian laser modes,” *Physical Review A*, Vol. 45, No. 11, 8185, 1992.

[2] Yang, Y., Y.-X. Ren, M. Chen, Y. Arita, and C. Rosales-Guzmán, “Optical trapping with structured light: A review,” *Advanced Photonics*, Vol. 3, No. 3, 034001, 2021.

[3] Forbes, A., M. D. Oliveira, and M. R. Dennis, “Structured light,” *Nature Photonics*, Vol. 15, No. 4, 253–262, 2021.

[4] Franke-Arnold, S., S. M. Barnett, M. J. Padgett, and L. Allen, “Two-photon entanglement of orbital angular momentum states,” *Physical Review A*, Vol. 65, No. 3, 033823, 2002.

[5] Guo, Z.-Y., S.-L. Qu, Z.-H. Sun, and S.-T. Liu, “Superposition of orbital angular momentum of photons by a combined computer-generated hologram fabricated in silica glass with femtosecond laser pulses,” *Chinese Physics B*, Vol. 17, No. 11, 4199, 2008.

[6] Zhang, C. and Y. Zhao, “Orbital angular momentum nondegenerate index mapping for long distance transmission,” *IEEE Transactions on Wireless Communications*, Vol. 18, No. 11, 5027–5036, 2019.

[7] Thidé, B., H. Then, J. Sjöholm, K. Palmer, J. Bergman, T. D. Carozzi, Y. N. Istomin, N. H. Ibragimov, and R. Khamitova, “Utilization of photon orbital angular momentum in the low-frequency radio domain,” *Physical Review Letters*, Vol. 99, No. 8, 087701, 2007.

[8] Tamburini, F., E. Mari, A. Sponselli, B. Thidé, A. Bianchini, and F. Romanato, “Encoding many channels on the same frequency through radio vorticity: First experimental test,” *New Journal of Physics*, Vol. 14, No. 3, 033001, 2012.

[9] Tamburini, F., E. Mari, B. Thidé, C. Barbieri, and F. Romanato, “Experimental verification of photon angular momentum and vorticity with radio techniques,” *Applied Physics Letters*, Vol. 99, No. 20, 204102, 2011.

[10] Bennis, A., R. Niemiec, C. Brousseau, K. Mahdjoubi, and O. Emile, “Flat plate for OAM generation in the millimeter band,” in *2013 7th European Conference on Antennas and Propagation (EuCAP)*, 3203–3207, Gothenburg, Sweden, 2013.

[11] Deng, C., W. Chen, Z. Zhang, Y. Li, and Z. Feng, “Generation of OAM radio waves using circular Vivaldi antenna array,” *International Journal of Antennas and Propagation*, Vol. 2013, No. 1, 847859, 2013.

[12] Wei, W., K. Mahdjoubi, C. Brousseau, and O. Emile, “Generation of OAM waves with circular phase shifter and array of patch antennas,” *Electronics Letters*, Vol. 51, No. 6, 442–443, 2015.

[13] Guo, Z.-G. and G.-M. Yang, “Radial uniform circular antenna array for dual-mode OAM communication,” *IEEE Antennas and Wireless Propagation Letters*, Vol. 16, 404–407, 2016.

[14] Zhang, W., S. Zheng, X. Hui, Y. Chen, X. Jin, H. Chi, and X. Zhang, “Four-OAM-mode antenna with traveling-wave ring-slot structure,” *IEEE Antennas and Wireless Propagation Letters*, Vol. 16, 194–197, 2016.

[15] Berry, M. V., “The adiabatic phase and pancharatnam's phase for polarized light,” *Journal of Modern Optics*, Vol. 34, No. 11, 1401–1407, 1987.

[16] Yu, N., P. Genevet, M. A. Kats, F. Aieta, J.-P. Tetienne, F. Capasso, and Z. Gaburro, “Light propagation with phase discontinuities: Generalized laws of reflection and refraction,” *Science*, Vol. 334, No. 6054, 333–337, 2011.

[17] Genevet, P., N. Yu, F. Aieta, J. Lin, M. A. Kats, R. Blanchard, M. O. Scully, Z. Gaburro, and F. Capasso, “Ultra-thin plasmonic optical vortex plate based on phase discontinuities,” *Applied Physics Letters*, Vol. 100, No. 1, 013101, 2012.

[18] Yu, S., L. Li, and N. Kou, “Generation, reception and separation of mixed-state orbital angular momentum vortex beams using metasurfaces,” *Optical Materials Express*, Vol. 7, No. 9, 3312–3321, 2017.

[19] Zhao, H., B. Quan, X. Wang, C. Gu, J. Li, and Y. Zhang, “Demonstration of orbital angular momentum multiplexing and demultiplexing based on a metasurface in the terahertz band,” *ACS Photonics*, Vol. 5, No. 5, 1726–1732, 2017.

[20] Wu, G.-B., K. F. Chan, K. M. Shum, and C. H. Chan, “Millimeter-wave holographic flat lens antenna for orbital angular momentum multiplexing,” *IEEE Transactions on Antennas and Propagation*, Vol. 69, No. 8, 4289–4303, 2021.

[21] Yao, Y., X. Liang, M. Zhu, W. Zhu, J. Geng, and R. Jin, “Analysis and experiments on reflection and refraction of orbital angular momentum waves,” *IEEE Transactions on Antennas and Propagation*, Vol. 67, No. 4, 2085–2094, 2019.

[22] Menzel, C., C. Rockstuhl, and F. Lederer, “Advanced jones calculus for the classification of periodic metamaterials,” *Physical Review A — Atomic, Molecular, and Optical Physics*, Vol. 82, No. 5, 053811, 2010.

[23] Chen, M. L. N., L. J. Jiang, and W. E. I. Sha, “Artificial perfect electric conductor-perfect magnetic conductor anisotropic metasurface for generating orbital angular momentum of microwave with nearly perfect conversion efficiency,” *Journal of Applied Physics*, Vol. 119, No. 6, 064506, 2016.

[24] Luukkonen, O., C. Simovski, G. Granet, G. Goussetis, D. Lioubtchenko, A. V. Raisanen, and S. A. Tretyakov, "Simple and accurate analytical model of planar grids and high-impedance surfaces comprising metal strips or patches," *IEEE Transactions on Antennas and Propagation*, Vol. 56, No. 6, 1624–1632, 2008.

[25] Barrera, M. A. R. and W. P. Carpes, "Bandwidth for the equivalent circuit model in square-loop frequency selective surfaces," *IEEE Transactions on Antennas and Propagation*, Vol. 65, No. 11, 5932–5939, 2017.

[26] Ferreira, D., R. F. S. Caldeirinha, I. Cuiñas, and T. R. Fernandes, "Square loop and slot frequency selective surfaces study for equivalent circuit model optimization," *IEEE Transactions on Antennas and Propagation*, Vol. 63, No. 9, 3947–3955, 2015.

[27] Langley, R. J. and E. A. Parker, "Equivalent circuit model for arrays of square loops," *Electronics Letters*, Vol. 18, No. 7, 294–296, 1982.

[28] Ran, Y., J. Liang, T. Cai, and H. Li, "High-performance broadband vortex beam generator using reflective Pancharatnam-Berry metasurface," *Optics Communications*, Vol. 427, 101–106, 2018.

[29] Chen, G.-T., Y.-C. Jiao, and G. Zhao, "A reflectarray for generating wideband circularly polarized orbital angular momentum vortex wave," *IEEE Antennas and Wireless Propagation Letters*, Vol. 18, No. 1, 182–186, 2019.

[30] Li, B., P. F. Jing, L. Q. Sun, K. W. Leung, and X. Lv, "3D printed OAM reflectarray using half-wavelength rectangular dielectric element," *IEEE Access*, Vol. 8, 142 892–142 899, 2020.

[31] Yu, Z.-Y., Y.-H. Zhang, and H.-T. Gao, "A high-efficiency and broadband folded reflectarray based on an anisotropic metasurface for generating orbital angular momentum vortex beams," *IEEE Access*, Vol. 9, 87 360–87 369, 2021.

[32] Ishfaq, M., X. Li, Z. Qi, W. Zhao, A. Aziz, L. Qiu, and S. Memon, "A transmissive metasurface generating wideband OAM vortex beam in the Ka-band," *IEEE Antennas and Wireless Propagation Letters*, Vol. 22, No. 8, 2007–2011, 2023.